Nanoscale

PAPER

View Article Online
View Journal | View Issue

Cite this: *Nanoscale*, 2014, **6**, 5999

Structural development of gold and silver nanoparticles within hexagonally ordered spherical micellar diblock copolymer thin films†

Chia-Min Chen, Yi-Jiun Huang and Kung-Hwa Wei*

The spatial arrangement of metal nanoparticle (NP) arrays in block copolymers has many potential applications in OFET-type memory devices. In this study, we adopted a trapping approach in which we used a monolayer thin film of polystyrene-*block*-poly(4-vinylpyridine) (PS_{56k}-*b*-$P4VP_{8k}$)—a highly asymmetric diblock copolymer having a spherical micelle morphology—to incorporate various amounts of one-phase-synthesized dodecanethiol-passivated silver (DT–Ag) NPs and a fixed amount of ligand-exchanged pyridine-coated gold (Py–Au) NPs into the polystyrene (PS) and poly(4-vinylpyridine) (P4VP) blocks, respectively. We characterized the packing of these metal NPs in the two blocks of the nanostructured diblock copolymer using reciprocal-space synchrotron grazing incidence small-angle X-ray scattering (GISAXS) as well as atomic force microscopy (AFM) and transmission electron microscopy (TEM) in the real space. The packing of the Ag NPs in the PS block was dependent on their content, which we tuned by varying the concentrations in the composite solution at a constant rate of spin-coating. The two-dimensional hierarchical arrangement of Ag and Au NPs within the BCP thin films was enhanced after addition of the Py–Au NPs into the P4VP block and after spin-coating a thinner film from a low concentration solution (0.1 wt%), due to the DT–Ag NPs accumulating around the Py–Au/P4VP cores; this two-dimensional hierarchical arrangement decreased at a critical DT–Ag NP weight ratio (*c*) of 0.8 when incorporating the Py–Au NPs into the P4VP domains through spin-coating at higher solution concentration (0.5 wt%), where the DT–Ag NPs realigned by rotating 20° along the *z* axis in the real space, due to oversaturation of the DT–Ag NPs within the PS domains.

Received 2nd January 2014
Accepted 20th March 2014

DOI: 10.1039/c4nr00020j

www.rsc.org/nanoscale

Introduction

The incorporation of metal nanoparticles (NPs) into diblock copolymers (BCPs) can provide composites displaying unique and useful electronic, optical, and magnetic properties. These properties, however, depend critically on the spatial distribution of the NPs within particular blocks, in turn depending on the dispersion of the NPs within the BCPs, itself being affected by the method used to prepare NPs. Metal NPs can be incorporated into one block of a BCP through *in situ* preparation methods,[1–6] where reduction of metal ions occurs in one of the block domains, or through *ex situ* preparation methods,[7–12] where surface ligands on the metal NPs interact with only one block of a diblock copolymer. *In situ* preparation methods can, however, lead to the coalescence of two or three micelles, thereby destabilizing them due to an excess or residual amount of the reducing agent; for example, hydrazine (N_2H_4) can deprotonate the pyridinium units and because it is polar, can reside selectively within the cores of the micelles, resulting in swelling.[13] Accordingly, several *ex situ* methods have been developed for selective incorporation of ligand-[7–9] and polymer-stabilized[10–12] metal NPs into the desired domains of BCPs.

Only a few studies of the incorporation of NPs into diblock copolymers have focused on controlling the assembly of two kinds of metal NPs within monolayer structures of diblock copolymer micelles.[14,15] Precise control over the spatial organization of these two types of metal NPs has typically been restricted by the metal NPs that were located in the entire matrix-domain.[16] For example, when the metal NP size is significantly less than the radius of gyration (R_g) of the copolymer blocks, the embedded metal NPs tend to segregate at the interface between the two dissimilar blocks of a diblock copolymer at thermal equilibrium; in contrast, when the metal NPs have a size approaching the value of R_g of the copolymer blocks, they tend to reside in the center zone of the embedded

Department of Materials Science and Engineering, National Chiao Tung University, 1001 Ta Hsueh Road, Hsinchu, 30050, Taiwan. E-mail: khwei@mail.nctu.edu.tw; Fax: +886-3-5724727; Tel: +886-3-5731771

† Electronic supplementary information (ESI) available: TEM images and corresponding size distributions of the TOP–Ag and Py–Ag NPs (Fig. S1); TEM images of the PS-*b*-(Py–$Ag_{1.0}$@P4VP) composite and EDX spectra recorded from the respective zones of the Au NPs (in the PS phase) and the Ag NPs (in the P4VP phase) within the (TOP–$Au_{1.0}$@PS)-*b*-(Py–$Ag_{1.0}$@P4VP) composite (Fig. S2) and representative AFM patterns of thin films of the (DT–$Ag_{0.6}$@PS)-*b*-P4VP and (DT–$Ag_{1.0}$@PS)-*b*-P4VP BCP/metal NP composite (Fig. S3). See DOI: 10.1039/c4nr00020j

block domains. Therefore, precise control over the sizes of metal NPs and over the spatial organization of the two types of metal NPs within BCP domains is very important not only for fabricating the BCP/metal NP composite thin films but also for taking advantage of their electronic properties in their applications.

Much attention has been focused recently on the development of BCP/metal NP composites, by incorporating various categories of metal NPs into well-ordered BCP monolayer films, for organic non-volatile memory (ONVM) applications (including resistor-,[17] capacitor-,[18–20] and OFET-type[21–23] memory devices) because of the tunable electron trapping ability of metal NPs and because various types of nanostructured BCPs can self-assemble with metal NPs into ordered structures. Among them, OFET-type memory devices comprising OFET devices with additional BCP/metal NP composite thin films as charge trapping layers can have much broader applications. For example, by embedding low-work-function Ag and high-work-function Pt NPs in the PS and P4VP blocks,[22] respectively, of a poly(styrene-*block*-4-vinylpyridine) (PS-*b*-P4VP) diblock copolymer monolayer thin film in an OFET-type memory device, one can induce positive and negative threshold voltage shifts for tuning the memory window in either the p- or n-channel. On the other hand, charge can be stored or erased in the trapping layer using the micellar nanostructured BCPs (asymmetric linear PS_{56k}-*b*-$P4VP_{8k}$, P4VP-core, and PS-shell) to act as discrete charge storage centers by applying gate voltages with different biases, and OFETs exhibit a tunable memory window since the PS shells in the lateral direction decreased upon increasing the layer thickness in a previous report.[24] However, the degradation of device properties and variation in the device-to-device performance of OFET-type memories using BCP/metal NP composites are often observed in our previous reports due to high loadings of metal NPs[22] and/or high-density BCP micelles upon increasing BCP solutions (0.1 up to 0.5 wt%)[24] making them more prone to change the ordered arrangement of metal NPs in the desired domains of BCP/metal NP composites and originally ordered nanostructured BCPs. For this reason, the successful use of BCPs as templates for BCP/metal NP composites will require control over both the ordered distribution and loading ratio of metal NPs within the target domains. Although higher loadings of metal NPs in BCP/metal NP composite thin films can result in larger memory windows for the corresponding OFET-type memory devices, they can also disrupt the high order of the BCP templates.[22,23] Therefore, one particularly difficult challenge has been the preparation of well-ordered BCP/metal NP composite systems that contain sufficient concentrations of NPs required for many practical device applications. Once achieved, these strategies would ideally be employed for solution-processing on flexible and roll-to-roll production stages.

In this paper, we report the critical spatial arrangement of two metal NP arrays—*ex situ*-synthesized dodecanethiol-passivated silver (DT–Ag) and pyridine-coated gold (Py–Au) NPs—in the respective blocks, by design, of a BCP. Through optimization of the loadings of the metal NPs and the concentrations of the BCP/metal NP composite solutions, we are able to form ordered BCP/metal NP composite thin films by co-operative self-assembly processes. The DT–Ag and Py–Au NPs were incorporated into the PS and P4VP blocks, respectively, of highly asymmetric PS_{56k}-*b*-$P4VP_{8k}$. We employed *ex situ* synthesis of Ag and Au NPs for this study so that they could be stabilized against agglomeration through grafting with surface ligands, thereby ensuring miscibility in the particular polymer domains. To control the sizes of the metal NPs and to ensure their incorporation into the desired BCP domains, we combined the modified one-phase synthesis of passivated metal NPs with ligand-exchange processes. Although the morphologies of BCP/metal NP composite thin films are commonly probed using transmission electron microscopy (TEM) and atomic force microscopy (AFM), these techniques provide only a localized view of structural information on the surface. Grazing-incidence small-angle X-ray scattering (GISAXS) is a powerful method for investigating the ordering and preferential orientation of thin films over an area of several square millimeters,[24–27] with the ability to unearth buried or inner structures within a film. GISAXS curves can, therefore, provide quantitative information regarding the formation and structural factors of BCP/metal NP composite thin films, thereby revealing nanostructural morphologies within the plane of an object deposited on a substrate. Accordingly, we used real-space techniques, AFM and TEM, and the reciprocal-space technique GISAXS to investigate the nanostructures present in the BCP/metal NP composite thin films as a result of micro-phase separation and the spatial arrangement of the two types of metal NPs. Our results suggest that such well-ordered BCP/metal NP composite thin films, featuring hierarchically arranged pairs of metal NPs within ordered BCP micelles, can have potential applications in OFET-type memory devices.

Experimental section

Preparation of metal NPs

1-Dodecanethiol ($C_{12}H_{25}SH$, 98%) and sodium borohydride ($NaBH_4$, 99%) were obtained from Acros. Trioctylphosphine (TOP, 90%) was purchased from Aldrich. Silver nitrate ($AgNO_3$) and pyridine (C_5H_5N, 99%) were obtained from Showa. Hydrogen tetrachloroaurate(III) trihydrate ($HAuCl_4 \cdot 3H_2O$) was purchased from Alfa Aesar. Toluene (99%), EtOH (99%), acetone (99%), and hexane (99%) were obtained from Tedia, USA. In the one-phase synthesis of trioctylphosphine-protected silver (TOP–Ag) NPs [or trioctylphosphine-protected gold (TOP–Au) NPs], the molar ratio of $AgNO_3$ (or $HAuCl_4 \cdot 3H_2O$) to TOP to $NaBH_4$ was 1 : 2 : 10. The $AgNO_3$ (15 mg mL^{-1}) or $HAuCl_4 \cdot 3H_2O$ (20 mg mL^{-1}) precursor was dissolved in EtOH under vigorous stirring. A solution of the TOP ligand in EtOH was added dropwise over 3 h to the EtOH solution of $AgNO_3$ (or $HAuCl_4 \cdot 3H_2O$) under vigorous stirring. The resulting solution was added dropwise to an EtOH solution saturated with $NaBH_4$ and stirred further for 24 h. The precipitated product was isolated through centrifugation and dried under vacuum at room temperature, followed by washing with toluene, and then several times with EtOH to remove any residual free ligands. The resulting TOP-protected Ag (TOP–Ag) [or TOP-protected Au

(TOP–Au)] NPs were dissolved in pyridine and heated at 65 °C for 6 h to obtain Py–Ag (or Py–Au) NPs, which were added dropwise into hexane, separated through centrifugation, and then dried under vacuum at room temperature. The final solids were collected and redissolved in pyridine. These Py–Ag and Py–Au NP preparations were used as sources for incorporating NPs physically into the cores of hexagonally ordered micelles.

For the one-phase synthesis of dodecanethiol-passivated Ag NPs, the molar ratio of $AgNO_3$ to DT to $NaBH_4$ was 1 : 1 : 10, with anhydrous EtOH as the solvent; the synthesis was conducted under ambient conditions. $AgNO_3$ (15 mg mL^{-1}) was dissolved in EtOH under vigorous stirring. A solution of the dodecanethiol ligand in EtOH was added dropwise to the EtOH solution of $AgNO_3$, causing the mixture to immediately turn a cyan color; the mixture was then stirred vigorously for 3 h. The resulting solution was added dropwise to a saturated solution of $NaBH_4$ in EtOH and stirred for 24 h. The precipitated product was isolated through centrifugation and then dried under vacuum at room temperature. The crude product was washed with hexane, reprecipitated in EtOH, and centrifuged to remove any residual free ligands; this process was repeated several times. The final solid was collected and then redissolved in toluene. These single-phase-synthesized DT–Ag NPs were used as a source for the incorporation of Ag NPs physically around the cores of hexagonally ordered micelles.

BCP/metal NP composites

Asymmetric linear polystyrene-*block*-poly(4-vinylpyridine) (PS-*b*-P4VP) was purchased from Polymer Source ($M_n^{PS} = 56$ kg mol^{-1}; $M_n^{P4VP} = 8$ kg mol^{-1}; and polydispersity index = 1.07 denoted herein as PS_{56k}-*b*-$P4VP_{8k}$). A pyridine solution containing 0.1 wt % PS_{56k}-*b*-$P4VP_{8k}$ and Py–Au NPs (of the same weight ratio as that of the P4VP block in the solution) was stirred vigorously and then dried under vacuum to provide the PS-*b*-(Py–$Au_{1.0}$@P4VP) composite, which was redispersed in toluene by stirring vigorously for 2 days. Subsequently, two toluene solutions of neat PS-*b*-P4VP and PS-*b*-(Py–$Au_{1.0}$@P4VP) composites were mixed with a toluene solution of the DT–Ag NPs, providing solutions containing a prescribed weight ratio of 1.0 for the total DT–Ag NPs and the PS blocks. On the other hand, toluene solutions of the PS-*b*-(Py–$Au_{1.0}$@P4VP) composites were mixed at various ratios with a toluene solution of the DT–Ag NPs, providing solutions containing prescribed weight ratios (c) of the total DT–Ag NPs to the PS blocks of 0.4, 0.6, 0.8, 1.0, 1.2, and 1.4. These final mixtures were cast to obtain the composites, either on carbon-coated Cu grids for TEM measurements or on SiO_2/Si substrates (5000 rpm, 60 s) for AFM and GISAXS measurements. All of the cast thin films were dried under vacuum at room temperature. The (TOP–$Au_{1.0}$@PS)-*b*-(Py–$Ag_{1.0}$@P4VP) composites were prepared using the same method.

TEM and AFM measurements

TEM images were recorded using an FEI T12 transmission electron microscope with a low-energy electron beam (120 keV) to provide sufficient contrast to distinguish the PS and P4VP domains in all of the BCP/metal NP composites, without heavy ion staining. TEM images of the TOP–Au, TOP–Ag, DT–Ag, Py–Ag, and Py–Au NPs on the flat, amorphous, carbon-coated Cu grids (200 mesh) were recorded using an FEI T12 microscope; HRTEM images and selected-area electron diffraction (SAED) patterns were recorded using a JEOL JEM-2100F apparatus. To determine the size distributions of the NPs, the diameters of at least 200 particles were measured per sample. AFM images of thin films were recorded using a Digital Instruments Nanoscope IIIa microscope equipped with a multi-mode head. The tapping mode was employed using nanosensor silicon tips with a resonance frequency of 130 kHz. Thin films were prepared from the solutions of the BCP/metal NP composites through spin-coating on SiO_2/Si substrates (5000 rpm, 60 s). Scanning was accomplished with a scanning rate of 1 Hz and an image resolution of 512 × 512 pixels.

GISAXS measurements

GISAXS measurements were performed at the SWAXS end-station of the BL23A1 beamline of the Taiwan light source at the National Synchrotron Radiation Research Center (NSRRC). The experimental GISAXS geometry is displayed in Fig. 1. Two sets of instrument configurations were used for the X-ray beam energy (14 and 8 keV) and sample-to-detector distance (1.8 and 5.0 m, respectively) to cover a wider scattering range. Several incident angles were used in the GISAXS measurements; the best GISAXS patterns, obtained with incident angles of 0.12 and 0.2°, were selectively analyzed. 2D GISAXS patterns were recorded using a 2D MAR-CCD detector (MAR 135) with a frame size of 1024 pixels × 1024 pixels positioned at the end of a vacuum flight tube. The GISAXS profiles were obtained from the GISAXS patterns along the in-plane direction q_x with a fixed value of q_z at the specular beam position; q_x and q_z are the components of the scattering wave vector (defined by $4\pi\lambda^{-1}\sin\theta$, with the

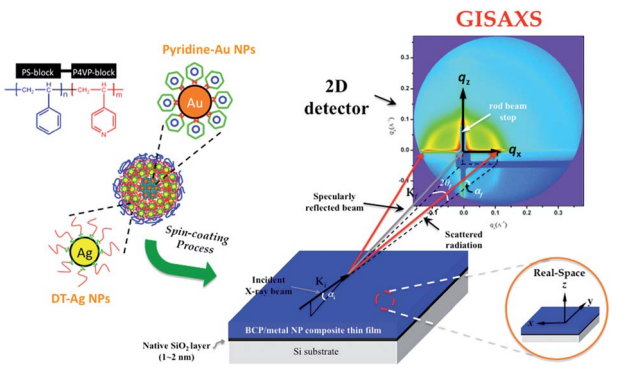

Fig. 1 Schematic representation of the experimental GISAXS setup for analyzing the BCP/metal NP composite thin films featuring micelle structures. The incident beam impinged on the sample surface at a grazing angle α_i; α_f and $2\theta_f$ are the exit angles of the X-ray beam with respect to the film surface and to the plane of incidence, respectively; k_i and k_f are the wave vectors of the incident and exit X-ray beams, respectively; q_x, q_y, and q_z are the components of the scattering vector q; a strip-shaped beam stop was used to block the strong specular reflection of the X-ray beam and diffuse scattering along the α_f axis. The intensity was monitored using a 2D detector in the x–z plane.

scattering angle $2\theta_f$) in the in-plane and out-of-plane directions, respectively.

Results and discussion

a. BCP/metal NP composites and local surface structures

The two-phase Brust–Schiffrin synthesis[28] is one of the most popular synthesis schemes for preparing metal NPs; the size distributions of metal NPs prepared using this method are, however, broad, generally requiring some type of post-synthesis treatment (*e.g.*, ligand exchange or thermal annealing) to decrease the size distribution. In addition, the presence of residual tetraoctylammonium bromide (TOABr)[29,30] can result in unusual self-organization properties and the formation of ring and line nanoscale patterns. A low polydispersity in the particle size is preferable when preparing self-assembled BCP/metal NP composite thin films. In this present study, we synthesized the dodecanethiol-modified silver (DT–Ag) and trioctylphosphine-modified gold (TOP–Au) NPs using a modified one-phase method—a combination of the syntheses methods described by Kim *et al.*[31] and Miyake *et al.*[32]—that has the advantages of minimizing the persistent ionic contamination from the residual phase transfer catalyst and decreasing the broad polydispersity in particle size while retaining the versatility associated with the two-phase Brust–Schiffrin synthesis. Because TOP–Au NPs are not compatible with the P4VP domains, we subjected the TOP–Au NPs to ligand exchange to produce Py–Au NPs, using a method we have described previously.[22,33] In summary, we have combined the modified one-phase method with ligand-exchange systems for synthesizing *ex situ* metal NPs and the integrated approach has been developed to exchange selectively incorporate metal NPs into the desired BCP domains. For example, Fig. S1† displays the TEM images of TOP–Au, Py–Ag NPs and PS-*b*-(Py–$Ag_{1.0}$@P4VP) composites; energy-dispersive X-ray (EDX) spectra for the TEM image of (TOP–$Au_{1.0}$@PS)-*b*-(Py–$Ag_{1.0}$@P4VP) composites confirmed that Ag and Au NPs were located in the P4VP cores and the PS matrix, respectively, of the copolymer in Fig. S2.†

Fig. 2 presents TEM images of the TOP–Au, DT–Ag, and Py–Au NPs we obtained after performing the modified one-phase syntheses and ligand exchange processes; Fig. 2a presents the 2D super-lattice of TOP–Au NPs that formed as a result of strong van der Waals attractive forces between the Au NPs, with a standard deviation of 0.14 nm from the averaged size of 4 nm (see Fig. 2c) indicating good control over the size distribution of these NPs. We calculated the mean diameter and standard deviation of the TOP–Au NPs by counting 200 particles from the TEM images recorded at a magnification of 650 000 times. Fig. 2b presents the crystal structure of the TOP–Au NPs determined through high-resolution TEM, with the SAED pattern in the inset; the strongest peak is homologous to the (111) and (222) facets of Au corresponding to the face-centered cubic (fcc) structure of Au, indicating that the Au NPs have the same structure as that of bulk Au. Fig. 2d and e display TEM images of the DT–Ag and Py–Au NPs, revealing mean diameters of 3.9 and 4.6 nm (not including ligands), respectively, with standard deviations of 0.3 and 0.4 nm, respectively.

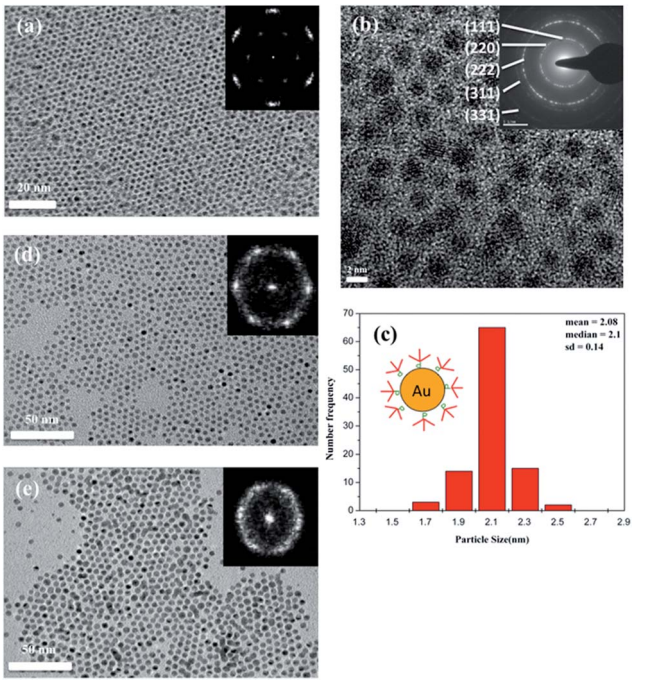

Fig. 2 (a) TEM image of the TOP–Au NPs; inset: fast Fourier transform (FFT) of the image, demonstrating a high degree of local order. (b) HRTEM image of the TOP–Au NPs; inset: diffraction pattern ring. (c) Corresponding size distribution of the TOP–Au NPs; inset: chemical structure of the TOP–Au NPs. (d and e) TEM images of (d) DT–Ag and (e) Py–Au NPs (dark spots); insets: corresponding FFTs.

In a selective solvent, the asymmetric PS_{56k}-*b*-$P4VP_{8k}$ diblock copolymer forms nanometer-sized micelles featuring an insoluble core and a soluble corona that is suitable for incorporating NPs. Therefore, we prepared the (DT–Ag_c@PS)-*b*-(Py–$Au_{1.0}$@P4VP) composites by first mixing Py–Au NPs and PS-*b*-P4VP in pyridine and then drying to form PS-*b*-(Py–$Au_{1.0}$@P4VP) composites. Subsequently, we added the DT–Ag NPs at various weight ratios (c) to the solution of PS-*b*-(Py–$Au_{1.0}$@P4VP) in toluene to form composite solutions of various compositions which were used to prepare thin films (see the Experimental section for detailed information). Herein, the subscripted number (c) represents the weight ratio of the embedded DT–Ag NPs in the PS block to the PS block. Fig. 3a–c display TEM images of the neat diblock copolymer and the BCP/metal NP composites. Fig. 3a and b reveal that the sizes of the Py–Au/P4VP composite cores (*ca.* 40 nm) were much larger than those of the neat P4VP cores (*ca.* 25 nm), indicating the successful incorporation of the Py–Au NPs into the P4VP cores. Fig. 3c reveals that the DT–Ag NPs were dispersed rather uniformly over the entire PS phase that surrounded the Py–Au/P4VP cores of the copolymer in the film. Therefore, the TEM images of the PS-*b*-(Py–$Au_{1.0}$@P4VP) and (DT–$Ag_{1.0}$@PS)-*b*-(Py–$Au_{1.0}$@P4VP) composites confirmed the concomitant sequestration of Au and Ag NPs into the P4VP and PS blocks, respectively, of highly asymmetric PS_{56k}-*b*-$P4VP_{8k}$ monolayer films. Fig. 3d–f display the AFM height images of the films of neat PS_{56k}-*b*-$P4VP_{8k}$, PS-*b*-(Py–$Au_{1.0}$@P4VP), and (DT–$Ag_{1.0}$@PS)-*b*-(Py–$Au_{1.0}$@P4VP). Fig. 3d presents the hexagonal packing of P4VP cores with a

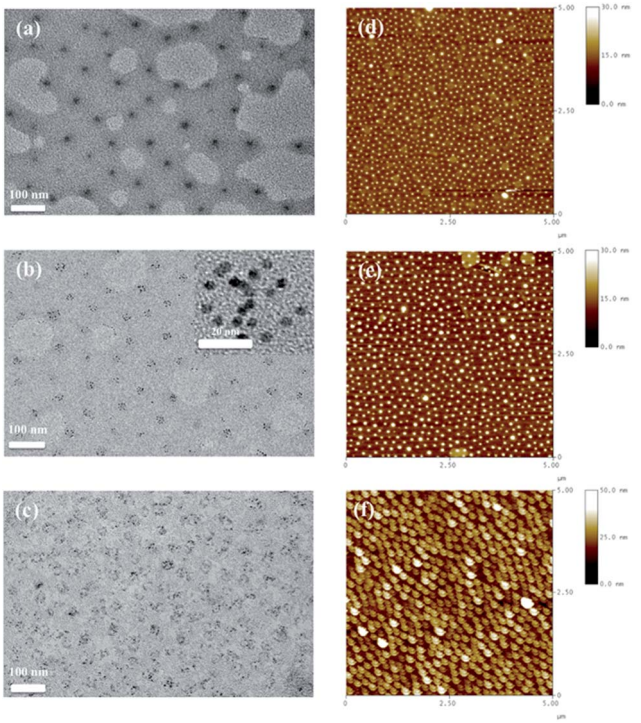

Fig. 3 (a–c) TEM images of the (a) PS_{56k}-*b*-$P4VP_{8k}$, (b) PS-*b*-(Py–$Au_{1.0}$@P4VP), and (c) (DT–$Ag_{1.0}$@PS)-*b*-(Py–$Au_{1.0}$@P4VP) composites. The dark spots in (a) and the light spots in (b) and (c) represent P4VP cores, in the absence and presence of Py–Au NPs; the dark spots in (b) and (c) represent the Py–Au NPs. Inset of (b): detailed view of single Py–Au/P4VP cores and their surroundings. (d–f) Representative AFM patterns of (d) the neat PS_{56k}-*b*-$P4VP_{8k}$ thin film and (e) the PS-*b*-(Py–$Au_{1.0}$@P4VP) and (f) (DT–$Ag_{1.0}$@PS)-*b*-(Py–$Au_{1.0}$@P4VP) BCP/metal NP composite thin films. Bright spots (local high lands) in (d) and (e) represent P4VP and Py–Au/P4VP cores, respectively. Bright zones (local high lands) and bright spots (2D hexagonal packing) in (f) represent Py–Au NPs and Py–Au/P4VP cores, respectively.

mean distance of 156 nm in the PS matrix with long-range order in a PS_{56k}-*b*-$P4VP_{8k}$ film prepared without annealing. The P4VP cores in this structure had an average diameter of 35 ± 5 nm and retained a hemispherical cap shape comprising a P4VP core and a PS shell.[24,34] Fig. 3e reveals that the long-range ordered structure of the PS-*b*-(Py–$Au_{1.0}$@P4VP) composite film was perturbed after we had incorporated a substantial number of Py–Au NPs into the P4VP cores; indeed, the hexagonal packing of the P4VP cores was altered. The diameter of the main Py–Au/P4VP cores along with the surrounding PS chains increases to 73.1 ± 7.4 nm and for PS-*b*-(Py–$Au_{1.0}$@P4VP) from 34.6 ± 5.4 nm for P4VP with surrounding PS chains for neat PS_{56k}-*b*-$P4VP_{8k}$, due to the selective incorporation of the Py–Au NPs into the P4VP phase and the swelling induced by the loading of the Py–Au NPs, consistent with the TEM data. In Fig. 3f, the bright spots (2D hexagonal packing) represent Py–Au/P4VP cores; the larger and smeared bright spots for the (DT–$Ag_{1.0}$@PS)-*b*-(Py–$Au_{1.0}$@P4VP) composite film may have resulted from oversaturated DT–Ag NPs accumulating around the Py–Au/P4VP cores. The presence of DT–Ag NPs also led to realignment of the Py–Au/P4VP cores in the PS matrix.

The preferred positioning of the smaller DT–Ag NPs near the inter-junction of the two dissimilar blocks in the large PS matrix phase is consistent with theoretical predictions.[35–37] The critical features indicate that DT–Ag NPs can either induce stretching of nearby PS chains or compressing of the P4VP cores that were surrounded by them. Hence, we attribute the sequestration of the two different types of metal NPs into their respective blocks of the diblock copolymer to (i) the modified one-phase synthesis of passivated metal NPs with low polydispersity in particle size and (ii) a trapping strategy employing a highly asymmetric diblock copolymer featuring a spherical morphology, as described in more detail in our previous report.[22] To gain a better understanding of the well-ordered BCP/metal NP nanocomposite thin films, we further used GISAXS to elucidate the spatial arrangement of the metal NP arrays in the sequestered BCP domains prepared at various metal NP loadings and under different depositing solution concentrations.

b. Nanostructures inside the BCP/metal NP composite thin films

The structures of the diblock copolymer composite thin films sequestering the two kinds of metal NPs depended on the loading of the metal NPs into the PS domains at a certain film thickness when the concentration of the composite solution was fixed at 0.1 wt%. Structural information in the in-plane and out-of-plane directions of the composite thin films was readily decipherable using GISAXS. Here, we focus on the in-plane direction of the BCP/metal NP composite film to understand the changes in the lateral and inner structures present in the composite thin films and in the lateral packing of the metal NPs in the respective blocks of the diblock copolymer films. The scattering peaks in the lower- and higher-q_x regions of the in-plane scattering provide information relating to the lateral spacing of the hexagonally ordered micelle cores and the short-range-ordered DT–Ag NPs, respectively. We obtained a certain degree of depth resolution by varying the angle of incidence of the X-ray beam and, thus the penetration depth. In our systems, the incident angles of the X-ray beam (α_i) for the lower- and higher-q_x regions were 0.12 and 0.2°, respectively.

Lower-q_x region. Fig. 4 displays the GISAXS patterns and in-plane profiles of (DT–Ag_c@PS)-*b*-(Py–$Au_{1.0}$@P4VP) films prepared at various DT–Ag NPs weight ratios (*c*), but with a fixed weight ratio (1.0) of Au NPs embedded in the P4VP block. All of the 2D GISAXS patterns reveal two observable symmetric sets of narrow Bragg diffraction streaks parallel to the out-of-plane direction (q_z) in the scattering pattern. The GISAXS profile of the neat PS_{56k}-*b*-$P4VP_{8k}$ thin film is consistent with that expected for 2D hexagonal packing and features three side maxima (denoted as I, II, and III) in Fig. 4i. Because of the high degree of order of the array (first-, second-, and third-order Bragg peaks and no Kiessig fringes), the neat PS_{56k}-*b*-$P4VP_{8k}$ thin film prepared without any metal NPs comprised highly ordered, hexagonally packed, hemispherical-cap-shaped P4VP cores in the PS matrix.[24] The incorporation of only Py–Au NPs into the P4VP cores in the composite thin film did not destroy the orientation of the P4VP cores: two side maxima remained

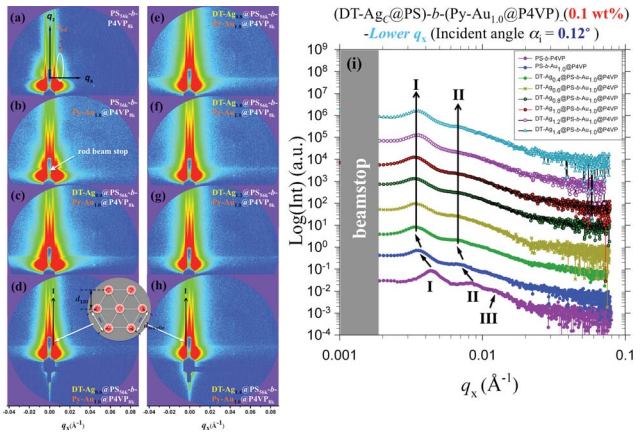

Fig. 4 (a–h) 2D GISAXS patterns and (i) in-plane GISAXS profiles of the (a) neat PS_{56k}-*b*-$P4VP_{8k}$ thin film and of (b–h) thin films of the (DT–Ag_c@PS)-*b*-(Py–$Au_{1.0}$@P4VP) composites incorporating Py–Au and DT–Ag NPs, with weight ratios of the latter (*c*) of (b) 0, (c) 0.4, (d) 0.6, (e) 0.8, (f) 1.0, (g) 1.2, and (h) 1.4. In (a), q_x and q_z are the in-plane and out-of-plane components of the momentum transfer vector *q*, respectively. The peaks of the structure factor, denoted as I, II, and III, arose from the micelle-to-micelle distance, $d_{micelle}$. The arrows in the in-plane profiles indicate scattering peaks from the hexagonally ordered copolymer micelle cores in the lower-q_x region. Insets of (d) and (h): curves analyzed using a 2D hexagonal lattice function.

clearly visible in the GISAXS pattern of the corresponding sample. Interestingly and most importantly, however, changes occurred to the positions of peaks I and II. As revealed in Fig. 4i, both peaks shifted toward lower values of q_x, as a result of a change in lateral spacing among the P4VP cores of the micelles. We estimated the mean spacing [$d_{micelle} = (4/3)^{1/2} d_{100}$] between the micelles, defined as the center-to-center distance between two neighboring micelles, from the first peak positions;[24,38] the two peaks displayed by the GISAXS profile of the PS-*b*-(Py–$Au_{1.0}$@P4VP) film shifted toward a lower value of q_x—or an increase in the value of $d_{micelle}$ to 205 nm (at $q_x = 0.003546$ Å^{-1}) from 169 nm (at $q_x = 0.004305$ Å^{-1})—relative to that of neat PS_{56k}-*b*-$P4VP_{8k}$ as a result of sequestration of the Py–Au NPs in the P4VP cores. Hence, the corresponding structure factor, arising from the lateral spacing among the P4VP cores of micelles, shifted toward a lower value of q_x in reciprocal space as the value of $d_{micelle}$ increased. The incorporation of only Py–Au NPs into the P4VP cores already led to lateral swelling of the domains of P4VP.

The GISAXS data were consistent with the representative AFM images of the neat PS_{56k}-*b*-$P4VP_{8k}$ and PS-*b*-(Py–$Au_{1.0}$@P4VP) composite thin films in Fig. 3d and e, respectively. As observed using AFM, the value of $d_{micelle}$ of PS-*b*-(Py–$Au_{1.0}$@P4VP) composite thin films increased (*cf.* Fig. 3d and e) and the micellar structure was not as ordered as those of the neat PS_{56k}-*b*-$P4VP_{8k}$ thin films, thereby producing a broadly distributed peak of the second order and resulting in the absence of the third order peak in the GISAXS profiles in Fig. 4i. When we added DT–Ag NPs with a weight ratio (*c*) of 0.4 into the PS domains of the PS-*b*-(Py–$Au_{1.0}$@P4VP) thin film, the Bragg diffraction streaks in the in-plane GISAXS profiles shifted slightly to lower values of q_x in the system. Further increasing the DT–Ag weight ratio (*c*) continuously in steps to 1.4, the 2D GISAXS patterns of the resulting (DT–Ag_c@PS)-*b*-(Py–$Au_{1.0}$@P4VP) composite thin films ($c = 0.6$, 0.8, 1.0, 1.2, and 1.4) shown in Fig. 4c–h reveal similar hexagonally ordered features and hexagonal packing with a mean distance of 220 nm (at $q_x = 0.003292$ Å^{-1}; indicated in Fig. 4i with two black arrows); in addition, the positions of peaks I and II remained unchanged in the GISAXS profiles. We presume that the increases in the values of $d_{micelle}$ in this stage were due to stretching of the PS chains induced by the presence of DT–Ag NPs.

To determine the influence of the DT–Ag NP loading on the PS domains on the Py–Au/P4VP-core orientation, we compared the properties of the (DT–Ag_c@PS)-*b*-P4VP composite thin films prepared without incorporating the Py–Au NPs into the P4VP domains. The 2D GISAXS patterns in Fig. 5a–f are quite similar, featuring one observable symmetric set of narrow Bragg diffraction streaks parallel to the q_z direction in the scattering pattern. The GISAXS profiles of the (DT–Ag_c@PS)-*b*-P4VP composite thin films in Fig. 5g are consistent with those expected for 2D hexagonal packing and feature two side maxima (denoted as I and II). In contrast, when loading the DT–Ag NPs at a weight ratio (*c*) of 0.4 into the PS domains of the neat PS_{56k}-*b*-$P4VP_{8k}$ thin film in the system, the Bragg diffraction streaks in the in-plane GISAXS profiles shifted slightly to the higher value of q_x of 0.004052 Å^{-1} [$D = 179$ nm; *cf.* the value of $d_{micelle}$ of the PS-*b*-(Py–$Au_{1.0}$@P4VP) composite thin film]. After further increasing the DT–Ag weight ratio (*c*) in steps from 0.6 to 1.0, we obtained 2D GISAXS patterns for the (DT–Ag_c@PS)-*b*-P4VP composite thin films (Fig. 5b–d) with similar hexagonally ordered features and values of $d_{micelle}$ (Fig. 5g) of 179, 169, and 164 nm, respectively. Thus, the values of $d_{micelle}$ became smaller, presumably because of the DT–Ag NPs accumulating around the P4VP cores and pressing into the P4VP cores.

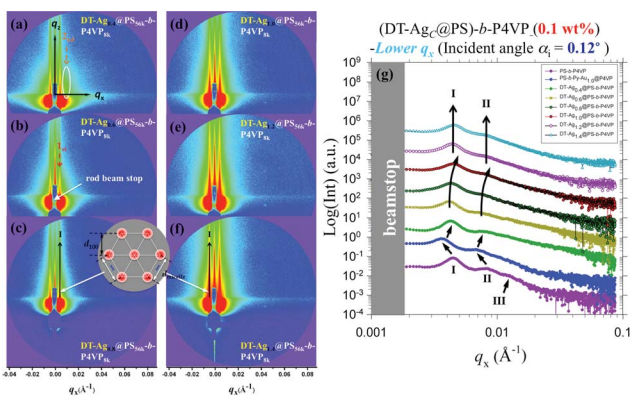

Fig. 5 (a–f) 2D GISAXS patterns and (g) in-plane GISAXS profiles of the (DT–Ag_c@PS)-*b*-P4VP composites incorporating DT–Ag NPs with weight ratios of the latter (*c*) of (a) 0.4, (b) 0.6, (c) 0.8, (d) 1.0, (e) 1.2, and (f) 1.4. In (a) q_x and q_z are the in-plane and out-of-plane components of the momentum transfer vector *q*, respectively. The peaks of the structure factor, denoted as I, II, and III, arose from the micelle-to-micelle distance, $d_{micelle}$. The arrows in the in-plane profiles indicate scattering peaks from the hexagonally ordered copolymer micelle cores in the lower-q_x region.

Fig. S3a and S3b† display representative AFM images of (DT–$Ag_{0.6}$@PS)-*b*-P4VP and (DT–$Ag_{1.0}$@PS)-*b*-P4VP composite thin films that were similar to the corresponding samples used to obtain the GISAXS measurement. Obviously, the micelle spacing was abridged because of the DT–Ag NPs accumulating around the P4VP cores and pressing into the P4VP cores. Moreover, when the weight ratio (c) increased to 1.2 and 1.4, the scattering peaks corresponding to the hexagonal packing of the micelle cores reverted back to the original positions (at q_x = 0.004052 Å^{-1}; D = 179 nm). We attribute the increase in the value of $d_{micelle}$ in this stage to stretching of the PS chains induced by the further addition of the DT–Ag NPs. Therefore, the almost constant values of $d_{micelle}$ (or of the scattering peak positions) of these (DT–Ag_c@PS)-*b*-(Py–$Au_{1.0}$@P4VP) composite thin films implied that the added DT–Ag NPs were all accommodated in the PS phase, forming more-homogeneous complex blocks.

Higher-q_x region. Fig. 6 displays a series of DT–Ag NP weight ratio-dependent GISAXS patterns and profiles of detailed log scans recorded for the in-plane scattering peak in the higher-q_x region for the neat PS_{56k}-*b*-$P4VP_{8k}$ thin film and the (DT–Ag_c@PS)-*b*-(Py–$Au_{1.0}$@P4VP) composite thin films. The related structure factor peak, denoted as IV, in Fig. 6i represents the interparticle distance (d_{np}) between two neighboring DT–Ag NPs. When the DT–Ag NP weight ratio (c) was 0.4 in the PS matrix, the lateral distance corresponding to this peak position indicated that the DT–Ag NPs formed a liquid-like ordering with a mean distance of approximately 5.9 nm (at q_x = 0.122 Å^{-1}), because the corresponding mean spacing was slightly lower than the average diameter of the DT–Ag NPs (*ca.* 6.3 nm; *i.e.*, a Ag NP core having a diameter of *ca.* 3.9 nm and a ligand shell thickness of *ca.* 1.2 nm). When we increased the value of c to 0.6, the DT–Ag NPs underwent a change in short-range ordering in the PS phase and decreased the value of d_{np} between two neighboring DT–Ag NPs, as revealed by the sharpening of the peak at a value of q_x of 0.123 Å^{-1} in Fig. 6i; concomitantly, the nearly constant value of $d_{micelle}$ implied that the added DT–Ag NPs were all accommodated in the PS phase. The lower value of d_{np} arose from the DT–Ag NPs that formed DT–Ag NP clusters. Upon increasing the DT–Ag NP weight ratio (c) from 0.8 to 1.4, however, the in-plane scattering peak (IV) shifted continuously from a value of q_x of 0.122 to 0.120 Å^{-1} in Fig. 6i. The position of these peaks shifted toward a lower value of q_x and a higher value of d_{np} upon increasing the value of c. Fig. 7 presents the corresponding series of (DT–Ag_c@PS)-*b*-P4VP composite GISAXS patterns and profiles of the detailed log scans recorded for the in-plane scattering peak in the higher-q_x region. The 2D patterns in Fig. 7a–f resemble the phenomena observed for the (DT–Ag_c@PS)-*b*-(Py–$Au_{1.0}$@P4VP) composite thin films. Upon increasing the weight ratio of the DT–Ag NPs (c = 0.4–1.4) in Fig. 7g, the in-plane scattering peak (IV) shifted continuously from a value of q_x of 0.121 to 0.115 Å^{-1} in the GISAXS profiles of the (DT–Ag_c@PS)-*b*-P4VP composite thin films. We attribute the continuous increase in the values of d_{np} to the DT–Ag NPs arranged inside the PS domains with their lateral distance increasing. If the NPs did not arrange within the PS domains, we would expect the lateral distance between the DT–Ag NPs to decrease.

Based on all of these GISAXS data, we suggest that as the DT–Ag NPs loading weight ratio (c) increased, regardless of the incorporation or absence of the Py–Au NPs in P4VP domains, the DT–Ag NPs within the PS domains remained arranged regularly in the in-plane direction. Moreover, the hexagonal peaks in the low-q_x region for the array of micelles were especially enhanced when incorporating the Py–Au NPs into the P4VP domains, compared to those without Py–Au NPs in the P4VP domains, due to the DT–Ag NPs accumulating around and pressing into the P4VP cores. Thus, the DT–Ag NPs interacted

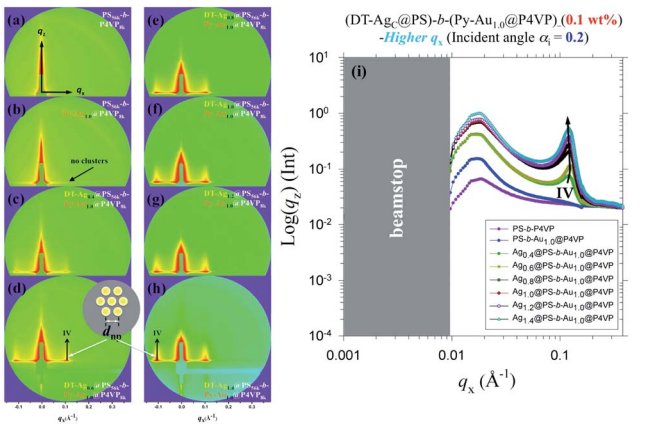

Fig. 6 (a–h) 2D GISAXS patterns and (i) in-plane GISAXS profiles for (a) the neat PS_{56k}-*b*-$P4VP_{8k}$ thin film and (b–h) thin films of the (DT–Ag_c@PS)-*b*-(Py–$Au_{1.0}$@P4VP) composites incorporating Py–Au and DT–Ag NPs with concentrations of the latter (c) of (b) 0, (c) 0.4, (d) 0.6, (e) 0.8, (f) 1.0, (g) 1.2, and (h) 1.4. In (a), q_x and q_z are the in-plane and out-of-plane components of the momentum transfer vector q, respectively. The intensity scale is logarithmic. The peaks of the structure factor, denoted as IV, arose from the mean interparticle distance, d_{np}, in the higher-q_x region.

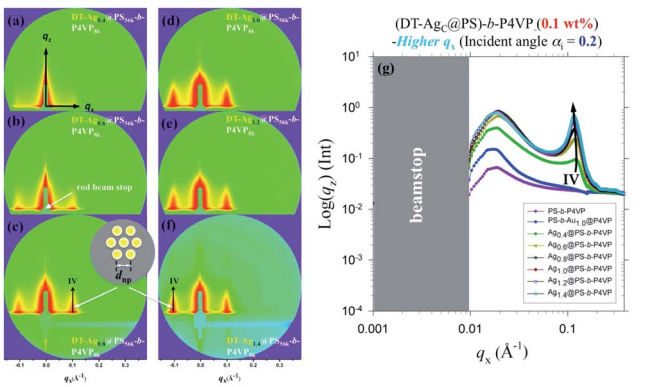

Fig. 7 (a–f) 2D GISAXS patterns and (g) in-plane GISAXS profiles of thin films of the (DT–Ag_c@PS)-*b*-P4VP composites incorporating DT–Ag NPs, with concentrations of the latter (c) of (a) 0.4, (b) 0.6, (c) 0.8, (d) 1.0, (e) 1.2, and (f) 1.4. In (a), q_x and q_z are the in-plane and out-of-plane components of the momentum transfer vector q, respectively. The intensity scale is logarithmic. The peaks of the structure factor, denoted as IV, arose from the mean interparticle distance, d_{np}, in the higher-q_x region.

collectively with the BCP (through their incorporation into the PS phase) and enhanced the ordering of the global structure in BCP/metal NP composite thin films. If the DT–Ag NPs had segregated from the copolymer, we would not have observed such interference in the scattering behavior between the DT–Ag NPs and the copolymer. Accordingly, optimized loadings (close to saturation) of the DT–Ag NPs in the PS blocks and of the Py–Au NPs in the P4VP blocks provided relatively homogenous complex blocks that were critical to forming the 2D hierarchical arrangement of Ag and Au NPs in the BCP/metal NP composite thin films.

c. High-density hexagonally packed arrangement in BCP/metal NP composite thin films

To understand the process leading to the spatial arrangement of the DT–Ag NPs in the PS domains, we observed the change in the hierarchical arrangement in the composite thin films upon increasing the solution concentration, with or without addition of the Py–Au NPs into the P4VP domains. In this system, we fixed the concentrations in all of the toluene solutions containing neat PS_{56k}-*b*-$P4VP_{8k}$ and the (DT–Ag_c@PS)-*b*-(Py–$Au_{1.0}$@P4VP) and (DT–Ag_c@PS)-*b*-P4VP composites at 0.5 wt%. Under these conditions, with AFM data alone it was difficult to interpret the spatial arrangement of the DT–Ag NPs within the BCP/metal NP thin films because AFM revealed only the local surface of the composite films. Therefore, we based our analysis on the GISAXS cross-sections of the composite thin films; the application of GISAXS allowed us to clarify whether any internal ordering of the composite films remained. The GISAXS patterns in the lower-q_x region (not shown here) of the thin films of the neat PS_{56k}-*b*-$P4VP_{8k}$ and of the BCP/metal NP composite prepared by spin-coating at solution concentrations of 0.5 wt% revealed that these thin films retained the hexagonally ordered features: a hemispherical-cap counter of the truncated spheres and lower values of $d_{micelle}$ (*cf.* those of the lower-concentration system prepared at 0.1 wt%). These results are consistent with our previous reports.[24] Moreover, in the absence of Py–Au NPs incorporated into the P4VP domains, we did not observe similar phenomena for the higher concentration (0.5 wt%) system with regard to the DT–Ag NPs accumulating around and pressing into the P4VP cores.

Fig. 8 presents the 2D GISAXS patterns and profiles of the thin films of neat PS_{56k}-*b*-$P4VP_{8k}$ and (DT–Ag_c@PS)-*b*-(Py–$Au_{1.0}$@P4VP) composites in the higher-q_x region. Before loading the DT–Ag NPs into the PS domains, the patterns of the PS_{56k}-*b*-$P4VP_{8k}$ and PS-*b*-(Py–$Au_{1.0}$@P4VP) thin films (Fig. 8a and b, respectively) did not feature any side-maximum peaks, but instead revealed further swelling of the P4VP domains induced by the addition of the Py–Au NPs. After adding the DT–Ag NPs into the PS domains (c = 0.4), the GISAXS profile of the (DT–$Ag_{0.4}$@PS)-*b*-(Py–$Au_{1.0}$@P4VP) composite thin film featured an additional side-maximum peak (denoted as V) in the higher-q_x region in-plane (Fig. 8i) and exhibited a weak ring pattern (so-called Debye–Scherrer ring) in the 2D pattern (Fig. 8c). The intensity of the ring around the specular peak in the 2D GISAXS patterns represents an equal distance (d_{np}) of approximately 4.9

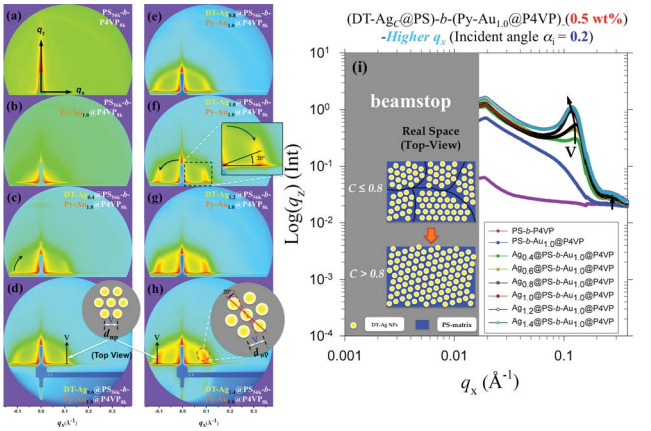

Fig. 8 (a–h) 2D GISAXS patterns and (i) in-plane GISAXS profiles for (a) the neat PS_{56k}-*b*-$P4VP_{8k}$ thin film and (b–h) thin films of the (DT–Ag_c@PS)-*b*-(Py–$Au_{1.0}$@P4VP) composites incorporating Py–Au and DT–Ag NPs spun from toluene solutions at concentrations of 0.5 wt%, with concentrations of the latter (c) of (b) 0, (c) 0.4, (d) 0.6, (e) 0.8, (f) 1.0, (g) 1.2, and (h) 1.4. In (a), q_x and q_z are the in-plane and out-of-plane components of the momentum transfer vector q, respectively. The intensity scale is logarithmic. The peaks of the structure factor, denoted as IV, arose from the mean interparticle distance, d_{np}, in the higher-q_x region.

nm (at q_x = 0.126 Å^{-1}) with the array of DT–Ag NPs oriented randomly along the q_z axis in the lateral plane. Upon increasing the weight ratio of the DT–Ag NPs (c = 0.6, 0.8) in the (DT–Ag_c@PS)-*b*-(Py–$Au_{1.0}$@P4VP) composite thin films, the intensity of the rings around this specular peak in the 2D GISAXS patterns became increasingly strong and more clearly visible (Fig. 8d and e, respectively); the position of peak V remained fixed, however, and the value of d_{np} did not increase. Further increasing the weight ratio of the DT–Ag NPs (c) in continuous steps to 1.4 caused the position of the peak V to shift toward lower values of q_x (from 0.126 to 0.117 Å^{-1}), while the value of d_{np} remained fixed near 5.4 nm. Moreover, the strong semi-circular ring was removed from the topmost part of the ring pattern and the specular peak was rotated by 20° along the q_y axis in the inset of Fig. 8f. The 20°-rotated arrays of DT–Ag NPs within the PS domains of the (DT–Ag_c@PS)-*b*-(Py–$Au_{1.0}$@P4VP) composite thin films (c > 0.8) were due to the DT–Ag NPs realigning inside the composite thin films along the plane q_{xy} in the reciprocal space.

Interestingly, in our GISAXS study of the (DT–Ag_c@PS)-*b*-P4VP composite thin films (Fig. 9), we observed an unexpected phenomenon for the arrangement of the DT–Ag NPs in the PS domains. The 2D GISAXS patterns of the (DT–Ag_c@PS)-*b*-P4VP composite thin films (c = 0.4–1.2) revealed several sharp reflected spots aligned in two rows along the q_z axis in Fig. 9a–e. These reflected spots suggest that the arrayed structures of the DT–Ag NPs inside the PS domains of the (DT–Ag_c@PS)-*b*-P4VP composite thin films were arranged with the two directional axes of the q_{xy} plane along the q_y axis and were packed spatially in a layer-by-layer manner along the q_z axis. They also indicated that well-ordered spatial arrangements of DT–Ag NPs were present within the PS domains of the (DT–Ag_c@PS)-*b*-P4VP

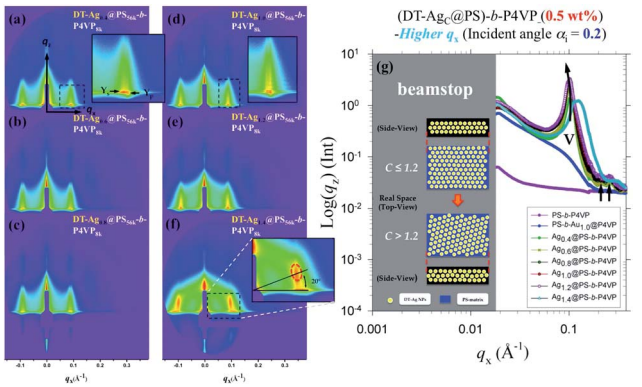

Fig. 9 (a–f) 2D GISAXS patterns and (g) in-plane GISAXS profiles for thin films of the (DT–Ag_c@PS)-*b*-P4VP composites spun from toluene solutions at a concentration of 0.5 wt%, with concentrations of the DT–Ag NPs (*c*) of (a) 0.4, (b) 0.6, (c) 0.8, (d) 1.0, (e) 1.2, and (f) 1.4. In (a), q_x and q_z are the in-plane and out-of-plane components of the momentum transfer vector *q*, respectively. Inset of (a): arrows marking the positions expected for the Yoneda peaks of the polymer (Y_P) and the Si substrate (Y_S). The intensity scale is logarithmic. The peaks of the structure factor, denoted as IV, arose from the mean interparticle distance, d_{np}, in the higher-q_x region.

composite thin films. In addition, the GISAXS profiles in Fig. 9g feature two sharp side-maximum peaks and weaker shoulder peaks along the q_x axis. These shoulder peaks confirmed that ordered arrays of DT–Ag NPs existed along the q_x axis in the q_{xy} plane. Therefore, the arrangement of the DT–Ag NPs in the q_{xy} plane was similar to a hexagonal array, with the array of DT–Ag NPs along the q_y axis featuring two competing directional axes. Upon increasing the DT–Ag NP weight ratio (*c*) in continuous steps to 1.4, however, the 2D pattern of the (DT–$Ag_{1.4}$@PS)-*b*-P4VP composite thin film returned to the ring pattern and the specular peak was rotated by 20° along the q_y axis. These features in the 2D pattern are similar to those for the (DT–Ag_c@PS)-*b*-(Py–$Au_{1.0}$@P4VP) composite thin films ($c = 1.0$–1.4). In addition, the position of the specular peak shifted toward a higher value of q_x (at $q_x = 0.125$ Å^{-1}), while the value of d_{np} remained fixed near 4.9 nm. We attribute this low value of d_{np} to the oversaturation of the DT–Ag NPs within the PS domains of the (DT–$Ag_{1.4}$@PS)-*b*-P4VP composite thin film, implying that the DT–Ag NPs lacked good spatial ordering along the q_z axis within the PS domains.

For the series of (DT–Ag_c@PS)-*b*-(Py–$Au_{1.0}$@P4VP) composite thin films in real space, these GISAXS data indicated that the DT–Ag NPs were arranged only within the PS domains of the (DT–Ag_c@PS)-*b*-(Py–$Au_{1.0}$@P4VP) composite thin films along the sample plane (*x*–*y* plane), but were not arranged spatially in the lateral order (*z* direction) during this stage of preparation. In addition, we identified two regimes for the spatial arrangement of the DT–Ag NPs within the PS domains (spun from solution at a concentration at 0.5 wt%) in the insets of Fig. 8i: (i) when the DT–Ag NP weight ratio (*c*) was less than or equal to 0.8, the array of DT–Ag NPs was randomly oriented in the sample plane (*x*–*y* plane) and produced a many-array domain in the PS matrix; (ii) when the DT–Ag NP weight ratio (*c*) was greater than 0.8, the array of DT–Ag NPs realigned in the sample plane by rotating 20° along the *z* axis in the real space. The reason that when the DT–Ag NP weight ratio (*c*) is greater than 0.8, the realignment of the array of DT–Ag NPs along the *z* axis takes place is that once the loading of the DT–Ag NP reaches the saturation point, the grain boundaries of local oriented NPs are broken, and a global orientation of the DT–Ag NPs occurs. In contrast to the series of (DT–Ag_c@PS)-*b*-P4VP composite thin films, the two regimes were confirmed in the insets of Fig. 9g: (i) we observed a spatially ordered arrangement of DT–Ag NPs along the *z* axis in the real space when the critical weight ratio (*c*) was less than or equal to 1.2; (ii) the spatially ordered arrangement disappeared and transferred to the 2D arrangement of the DT–Ag NPs along the *x*–*y* plane in the PS matrix when the critical weight ratio (*c*) was greater than 1.2. From the summary of the described GISAXS data above, we conclude that the metal NPs arranged themselves spontaneously within the hemispherical-cap counter of the truncated spheres as a result of selective affinity to their target domains during the microphase separation process.

Conclusions

We have demonstrated that the combination of (i) a modified one-phase synthesis route for controlling the size distribution of metal NPs and (ii) a designated trapping strategy employing a highly asymmetric BCP that forms spherical micelle structures is a useful approach for the preparation of well-ordered BCP/metal NP composite thin films over large areas. Using real-space AFM, TEM, and reciprocal-space GISAXS analysis techniques, our systematic investigation of the nanostructures formed through co-operative self-assembly of the two distinct kinds of metal NPs into BCP/metal NP composite thin films at various metal-to-NP weight ratios (*c*) and at various concentrations of the BCP/metal NP composites has highlighted the possibility of producing well-ordered spatial arrangements of metal NPs in desired BCP domains. In addition, we have found that the 2D hierarchical arrangements of Ag and Au NPs within the thin films of the well-ordered BCP/metal NP composites obtained through spin-coating at low solution concentration (0.1 wt%) were enhanced by adding the Py–Au NPs into the P4VP domains, due to the DT–Ag NPs accumulating around the Py–Au/P4VP cores; this order decreased when the DT–Ag NP weight ratio (*c*) extended beyond the critical value of 0.8 when incorporating the Py–Au NPs into the P4VP domains through spin-coating at a high solution concentration (0.5 wt%), where the DT–Ag NPs realigned (rotated by 20°) along the *z* axis in the real space, due to oversaturation of the DT–Ag NPs within the PS domains. Despite the low- (spun from 0.1 wt% solution) or high-density (spun from 0.5 wt% solution) of the hexagonally packed micellar arrangement, we suggest that such well-ordered BCP/metal NP composite thin film systems have potential applications in, for example, nonvolatile OFET-type memory devices.

Acknowledgements

This study was supported financially by the National Science Council (NSC 100-2221-E-009-022-MY3); we thank the National

Synchrotron Radiation Research Center, Taiwan, for supporting the GISAXS measurements.

Notes and references

1 J. P. Spatz, S. Sheiko and M. Möller, *Macromolecules*, 1996, **29**, 3220–3226.
2 J. P. Spatz, A. Roescher and M. Möller, *Adv. Mater.*, 1996, **8**, 337–340.
3 T. Hashimoto, M. Harada and N. Sakamoto, *Macromolecules*, 1999, **32**, 6867–6870.
4 J. P. Spatz, S. Mössmer, C. Hartmann, M. Möller, T. Herzog, M. Krieger, H.-G. Boyen, P. Ziemann and B. Kabius, *Langmuir*, 2000, **16**, 407–415.
5 N. Sakamoto, M. Harada and T. Hashimoto, *Macromolecules*, 2006, **39**, 1116–1124.
6 C. Mendoza, N. Gindy, J. S. Gutmann, A. Fromsdorf, S. Forster and A. Fahmi, *Langmuir*, 2009, **25**, 9571–9578.
7 M. R. Bockstaller, Y. Lapetnikov, S. Margel and E. L. Thomas, *J. Am. Chem. Soc.*, 2003, **125**, 5276–5277.
8 S. W. Yeh, K. H. Wei, Y. S. Sun, U. S. Jeng and K. S. Liang, *Macromolecules*, 2005, **38**, 6559–6565.
9 C. M. Huang, K. H. Wei, U. S. Jeng and K. S. Liang, *Macromolecules*, 2007, **40**, 5067–5074.
10 S. T. Selvan, J. P. Spatz, H. A. Klok and M. Möller, *Adv. Mater.*, 1998, **10**, 132–134.
11 J. J. Chiu, B. J. Kim, E. J. Kramer and D. J. Pine, *J. Am. Chem. Soc.*, 2005, **127**, 5036–5037.
12 K. Tsutsumi, Y. Funaki, Y. Hirokawa and T. Hashimoto, *Langmuir*, 1999, **15**, 5200–5203.
13 J. P. Spatz, S. Mößmer and M. Möller, *Chem.–Eur. J.*, 1996, **2**, 1552–1555.
14 B. H. Sohn, J. M. Choi, S. I. Yoo, S. H. Yun, W. C. Zin, J. C. Jung, M. Kanehara, T. Hirata and T. Teranishi, *J. Am. Chem. Soc.*, 2003, **125**, 6368–6369.
15 H. Acharya, J. Sung, B. H. Sohn, D. H. Kim, K. Tamada and C. Park, *Chem. Mater.*, 2009, **21**, 4248–4255.
16 A. Haryono and W. H. Binder, *Small*, 2006, **5**, 600–611.
17 W. I. Park, J. M. Yoon, M. Park, J. Lee, S. K. Kim, J. W. Jeong, K. Kim, H. Y. Jeong, S. Jeon, K. S. No, J. Y. Lee and Y. S. Jung, *Nano Lett.*, 2012, **12**, 1235–1240.
18 W. L. Leong, P. S. Lee, A. Lohani, Y. M. Lam, T. Chen, S. Zhang, A. Dodabalapur and S. G. Mhaisalkar, *Adv. Mater.*, 2008, **20**, 2325–2331.
19 J. S. Lee, Y. M. Kim, J. H. Kwon, H. Shin, B. H. Sohn and J. Lee, *Adv. Mater.*, 2009, **21**, 178–183.
20 J. S. Lee, Y. M. Kim, J. H. Kwon, J. S. Sim, H. Shin, B. H. Sohn and Q. Jia, *Adv. Mater.*, 2011, **23**, 2064–2068.
21 W. L. Leong, N. Mathews, S. Mhaisalkar, Y. M. Lam, T. Chen and P. S. Lee, *J. Mater. Chem.*, 2009, **19**, 7354–7361.
22 C. M. Chen, C. M. Liu, K. H. Wei, U. Jeng and C. H. Su, *J. Mater. Chem.*, 2012, **22**, 454–461.
23 Q. Wei, Y. Liu, E. R. Anderson, A. L. Briseno, S. P. Gido and J. J. Watkins, *ACS Nano*, 2012, **6**, 1188–1194.
24 C. M. Chen, C. M. Liu, M. C. Tsai, H. C. Chen and K. H. Wei, *J. Mater. Chem. C*, 2013, **1**, 2328–2337.
25 J. He, R. Tangirala, T. Emrick, T. P. Russell, A. Böker, X. Li and J. Wang, *Adv. Mater.*, 2007, **19**, 381–385.
26 M. S. Su, C. Y. Kuo, M. C. Yuan, U. Jeng, C. J. Su and K. H. Wei, *Adv. Mater.*, 2011, **23**, 3315–3319.
27 J. Rivnay, S. C. B. Mannsfeld, C. E. Miller, A. Salleo and M. F. Toney, *Chem. Rev.*, 2012, **112**, 5488–5519.
28 M. Brust, M. Walker, D. Bethell, D. J. Schiffrin and R. Whyman, *J. Chem. Soc., Chem. Commun.*, 1994, 801–802.
29 J. Fink, C. J. Kiely, D. Bethell and D. J. Schiffrin, *Chem. Mater.*, 1998, **10**, 922–926.
30 C. A. Waters, A. J. Mills, K. A. Johnson and D. J. Schiffrin, *J. Chem. Soc., Chem. Commun.*, 2003, 540–541.
31 S. Y. Kang and K. Kim, *Langmuir*, 1998, **14**, 226–230.
32 T. Teranishi, I. Kiyokawa and M. Miyaka, *Adv. Mater.*, 1998, **10**, 596–599.
33 C. P. Li, C. H. Wu, K. H. Wei, J. T. Sheu, J. Y. Huang, U. S. Jeng and K. S. Liang, *Adv. Funct. Mater.*, 2007, **17**, 2283–2290.
34 J. Y. Liou and Y. S. Sun, *Macromolecules*, 2012, **45**, 1963–1971.
35 M. R. Thompson, V. V. Ginzburg, M. W. Matsen and A. C. Balazs, *Science*, 2001, **292**, 2469–2472.
36 R. B. Thompson, V. V. Ginzburg, M. W. Matsen and A. C. Balazs, *Macromolecules*, 2002, **35**, 1060–1071.
37 J. Y. Lee, R. B. Thompson, D. Jasnow and A. C. Balazs, *Macromolecules*, 2002, **35**, 4855–4858.
38 A. Frömsdorf, A. Kornowski, S. Pütter, H. Stillrich and L. T. Lee, *Small*, 2007, **3**, 880–889.